

Non-contact atomic force microscopy study of hydroxyl groups on the spinel $\text{MgAl}_2\text{O}_4(100)$ surface

This article has been downloaded from IOPscience. Please scroll down to see the full text article.

2012 Nanotechnology 23 325703

(<http://iopscience.iop.org/0957-4484/23/32/325703>)

View [the table of contents for this issue](#), or go to the [journal homepage](#) for more

Download details:

IP Address: 130.233.204.250

The article was downloaded on 30/07/2012 at 13:38

Please note that [terms and conditions apply](#).

Non-contact atomic force microscopy study of hydroxyl groups on the spinel $\text{MgAl}_2\text{O}_4(100)$ surface

F Federici Canova^{1,2}, A S Foster^{1,2}, M K Rasmussen³, K Meinander³,
F Besenbacher³ and J V Lauritsen³

¹ Department of Physics, Tampere University of Technology, PO Box 692, FI-33010 Tampere, Finland

² Department of Applied Physics, Aalto University, PO Box 11100, FI-00076 Aalto, Finland

³ Interdisciplinary Nanoscience Center (iNANO), Aarhus University, Denmark

E-mail: filippo.federici@tut.fi

Received 28 March 2012, in final form 9 July 2012

Published 25 July 2012

Online at stacks.iop.org/Nano/23/325703

Abstract

Atom-resolved non-contact atomic force microscopy (NC-AFM) studies of the magnesium aluminate (MgAl_2O_4) surface have revealed that, contrary to expectations, the (100) surface is terminated by an aluminum and oxygen layer. Theoretical studies have suggested that hydrogen plays a strong role in stabilizing this surface through the formation of surface hydroxyl groups, but the previous studies did not discuss in depth the possible H configurations, the diffusion behaviour of hydrogen atoms and how the signature of adsorbed H is reflected in atom-resolved NC-AFM images. In this work, we combine first principles calculations with simulated and experimental NC-AFM images to investigate the role of hydrogen on the $\text{MgAl}_2\text{O}_4(100)$ surface. By means of surface energy calculations based on density functional theory, we show that the presence of hydrogen adsorbed on the surface as hydroxyl groups is strongly predicted by surface stability considerations at all relevant partial pressures of H_2 and O_2 . We then address the question of how such adsorbed hydrogen atoms are reflected in simulated NC-AFM images for the most stable surface hydroxyl groups, and compare with experimental atom-resolved NC-AFM data. In the appendices we provide details of the methods used to simulate NC-AFM using first principles methods and a virtual AFM.

(Some figures may appear in colour only in the online journal)

1. Introduction

Insulating metal oxides with the spinel structure are commonly available materials [1], and particularly useful in industrial applications such as ceramic technology and fuel cell materials [2]. Spinel structures are also very important in heterogeneous catalysis [3, 4], as the surface itself of some spinel-type oxides may be catalytically active [5, 6], and they are frequently used as a support for catalytically active nanoclusters [2–4]. Resolving the atomic structure of this class of insulating oxides, which is critical to understand their interesting properties, is experimentally challenging, due to their insulating nature: scanning tunnelling microscopy

(STM) cannot be operated and conventional surface science techniques suffer from charge accumulation on the sample. Furthermore, when truncating the bulk structure, quite often the resulting surface exhibits a large dipole that would normally trigger defect formation, surface reconstruction or adsorption in order for it to be compensated [7, 8], making assignment of the surface termination a far from simple task.

Magnesium aluminate (MgAl_2O_4) belongs to this class of materials [8–10], and until recently mainly theoretical studies have been applied to study its surface structure. The few experimental studies in the literature have provided little conclusive atomic-scale insight on the possible surface terminations [11–15]. However, more recently atom-

resolved non-contact atomic force microscopy (NC-AFM) measurements [16, 17], combined with density functional theory (DFT) calculations and NC-AFM simulations [18] were successfully applied in [19] to determine that the surface structure of $\text{MgAl}_2\text{O}_4(100)$ adopts the so-called $\text{O}_4\text{-Al}_4\text{-O}_4$ termination. It was furthermore found that this surface contained a considerable fraction of Mg–Al inversion defects, which were concluded to participate in the stabilization of the surface together with adsorption of hydrogen. Reference [20] reported a more detailed and exhaustive study of the NC-AFM contrast formation on the inversion defects and its distance dependence. Despite the good agreement observed between the two, some weaker features of the contrast measured around the defects could not be entirely explained and hydrogen adsorption was proposed in [20] as a possible cause. Hydroxyls are known to be present on the surface of high-surface-area spinels used in e.g. catalysis [21, 22], but a detailed atomic-scale understanding of hydroxyl species on the surface is absent. The configuration and bonding strength of such surface hydroxyls determine the so-called Brønsted basicity and acidity of such metal oxides, which in turn may determine the catalytic properties in hydrogenation reactions, the tendency of the metal oxide to sinter and its binding properties to metals. However, so far a fundamental relation between the Brønsted acid–base strength of an oxide and the atomistic properties of surface hydroxyls (coordination, bonding strength, diffusivity etc) is absent, and it is therefore interesting to investigate the nature of hydroxyl species on the atomic level. In this study, we therefore investigate the surface stability of different H adsorption sites with DFT calculations and compare the NC-AFM simulated images of the most stable configurations with the experimental ones. The simulation technique is furthermore described in detail in sections A and B, as we believe it to be important for future studies involving AFM simulations of adsorbates on surfaces.

2. Methods

Generally the applied methods in this work are the same as in the previously published studies [19, 20], but here we highlight some key aspects that are particular to this study or have not been explained in detail earlier.

2.1. Experiments

The NC-AFM experiments were performed in an ultra-high vacuum (UHV) chamber which is equipped with a combined STM/AFM microscope (Omicron VT-AFM/STM) capable of resolving the atomic structure of metal oxide surfaces in the non-contact AFM mode [23]. The details of our NC-AFM set-up and general parameters and procedures used for obtaining atomic resolution NC-AFM images on the $\text{MgAl}_2\text{O}_4(100)$ surface are given in our previous studies [19, 20]. All NC-AFM images reported in this study were recorded in the constant height mode at room temperature.

As described in detail in [19, 20], the standard preparation of a clean and flat (100) surface of MgAl_2O_4 involves Ar^+ sputtering followed by annealing at 1000–1050 °C in a $1 \times$

10^{-7} mbar O_2 atmosphere. Since this paper is concerned with the hydrogen content on the $\text{MgAl}_2\text{O}_4(100)$ surface, it is appropriate to discuss the role of H in the experiment further. During annealing of the sample in the oxygen gas, trace amounts of H_2 gas were always present in the vacuum system, corresponding to a partial pressure of hydrogen at a level up to 1×10^{-9} mbar as detected with a quadrupole mass spectrometer. It is therefore highly likely that some hydrogen is also present on the surface after this standard preparation, as concluded in [19] and seen for a range of other metal oxide surfaces studied under UHV conditions. Direct quantification of hydrogen on surfaces is, however, associated with significant challenges, since the standard technique for chemical analysis, x-ray photo-electron spectroscopy (XPS), is not directly sensitive to H [24]. We did monitor the surface composition by XPS using Mg $K\alpha$ radiation (Phoibos 100 analyser and XR 50 source, SPECS GmbH, Berlin, Germany), and the spectra revealed the presence of only Mg, Al and O. Hydrogen in the form of surface hydroxyl groups can in principle be quantified by resolving a shoulder on the O 1s XPS peak arising due the ~ 2 eV higher binding energy of O in a hydroxyl (OH) as compared with O (see e.g. [25, 26]). In our experiments, however, this analysis was inhibited by a rather large (3–4 eV) broadening of the O 1s peak due to uneven charging of the sampled area of the insulating surface. Additional experiments exposing the surface to higher pressures of H_2 or even annealing in a partial pressure of H_2 did not significantly change the appearance of the surface structure in NC-AFM images, indicating that H content on the surface was close to the saturation coverage even for standard preparation.

2.2. Surface energetics

All calculations in this work were performed using periodic plane-wave basis VASP code [27, 28], implementing the spin-polarized DFT and the generalized gradient approximation. Projected augmented wave (PAW) potentials [29, 30] were used to describe the core electrons. A kinetic energy cutoff of 450 eV was found to converge the total energy of the tip–surface systems to within 10 meV. Systematic k -point convergence was checked for smaller bulk and surface calculations, but for the large surface unit cell used in the NC-AFM simulations, the gamma point was sufficient. All diffusion calculations were determined using the climbing image nudged elastic band method [31].

The properties of the bulk and surface of MgAl_2O_4 were carefully checked within this methodology, and excellent agreement was achieved with experiments. A surface unit cell of $2 \times 2 \times 2$ was used (see figures 1 and 2) with a large vacuum gap, so that there was no artificial interaction between the tip and periodic images of the surface. The bottom layer of the surface was frozen to represent the bulk, while atoms in the upper layers were free to relax. This approach also provided effectively identical results to mirroring the surface on the top and bottom of the slab, and freezing the middle [19].

In order to predict surface terminations, we use the calculated surface energy as an indicator, with smaller energies predicting more stable surfaces. For non-stoichiometric

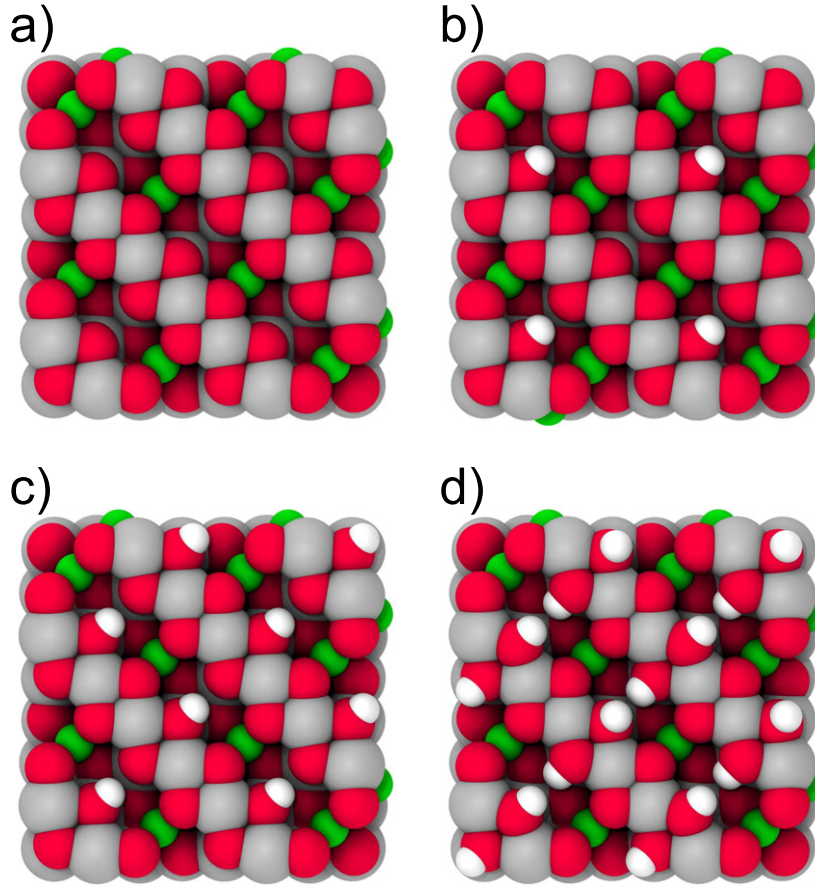


Figure 1. Atomic structures of the defect-free surface terminations of $\text{MgAl}_2\text{O}_4(100)$: (a) ideal surface with the $\text{O}_4\text{--Al}_4\text{--O}_4$ termination, (b) with 1 H, (c) with 2 H and (d) with 4 H per unit cell. The surfaces shown here represent the most stable configurations for the given amount of H adsorbed. Red atoms represents oxygen, grey is aluminum, green is magnesium and white represents hydrogen.

surfaces, the surface energy depends on the temperature and partial pressures of the surrounding gas atmosphere (O_2 and H_2). We use the chemical potential formalism, which has been used in numerous studies for other oxide materials (e.g. [32, 33]). One needs to choose sources for excess Al, Mg, O and for H in the case of hydrogen adsorption. As we have four different elements present (Mg, Al, O, H), we need four sources as references. We choose bulk MgAl_2O_4 spinel, O_2 and H_2 as three sources. However, the choice of the fourth source is not unique, as one can choose either MgO or $\alpha\text{-Al}_2\text{O}_3$ (or in the latter case, other phases of alumina, but we do not consider this choice here). We have performed the analysis for both MgO and $\alpha\text{-Al}_2\text{O}_3$ as reference, but found that the results depend very little on this choice. The surface energy (γ) is calculated as follows for MgO as a reference:

$$\gamma = \frac{1}{2} \left[E(\text{Mg}_{N_{\text{Mg}}} \text{Al}_{N_{\text{Al}}} \text{O}_{N_{\text{O}}} \text{H}_{N_{\text{H}}}) - \frac{N_{\text{Al}}}{2} E(\text{MgAl}_2\text{O}_4, \text{bulk}) \right] - \frac{1}{2} \left[\left(N_{\text{Mg}} + \frac{N_{\text{Al}}}{2} \right) E(\text{MgO}, \text{bulk}) + \left(N_{\text{O}} - \frac{3}{2} N_{\text{Al}} + N_{\text{Mg}} \right) \mu_{\text{O}} + N_{\text{H}} \mu_{\text{H}} \right] \quad (1)$$

where $E(\text{Mg}_{N_{\text{Mg}}} \text{Al}_{N_{\text{Al}}} \text{O}_{N_{\text{O}}} \text{H}_{N_{\text{H}}})$ is the energy of the surface structure with N_{Mg} Mg atoms, N_{Al} Al atoms, N_{O} O atoms and N_{H} H atoms. Furthermore, $E(\text{MgAl}_2\text{O}_4, \text{bulk})$ is the

energy for one formula unit of bulk spinel and $E(\text{MgO}, \text{bulk})$ is the energy for one formula unit of bulk magnesia. The chemical potential for oxygen is denoted μ_{O} and for hydrogen μ_{H} , which are determined from the temperature and partial pressures as follows:

$$\mu_{\text{O}} = \frac{1}{2} \mu_{\text{O}_2} = \frac{1}{2} \left[E_{\text{DFT}, \text{O}_2} + E_{\text{ZPE}, \text{O}_2} + \Delta H_{\text{O}_2}^{0, T} - T S_{\text{O}_2}^T + k_{\text{B}} T \ln \left(\frac{p(\text{O}_2)}{p_0} \right) \right] \quad (2)$$

where $E_{\text{DFT}, \text{O}_2}$ is the DFT energy of an isolated O_2 molecule, $E_{\text{ZPE}, \text{O}_2}$ is the zero-point energy of an O_2 molecule, $\Delta H_{\text{O}_2}^{0, T}$ is the enthalpy difference between 0 K and T , and S_{O_2} is the entropy at T . The zero-point energies, enthalpies and entropies are taken from thermodynamic tables [34]. p_0 is the standard pressure of 1 bar and p_{O_2} is the O_2 partial pressure taken from experimental conditions. The chemical potential for hydrogen is determined in a similar way.

These thermodynamic calculations comprise several approximations. First of all, we assume that the system is in thermodynamical equilibrium. This is not necessarily the case, since at low temperatures there might be kinetic barriers that hinder transition to the most favourable structure, and the AFM chamber is constantly evacuated, which is

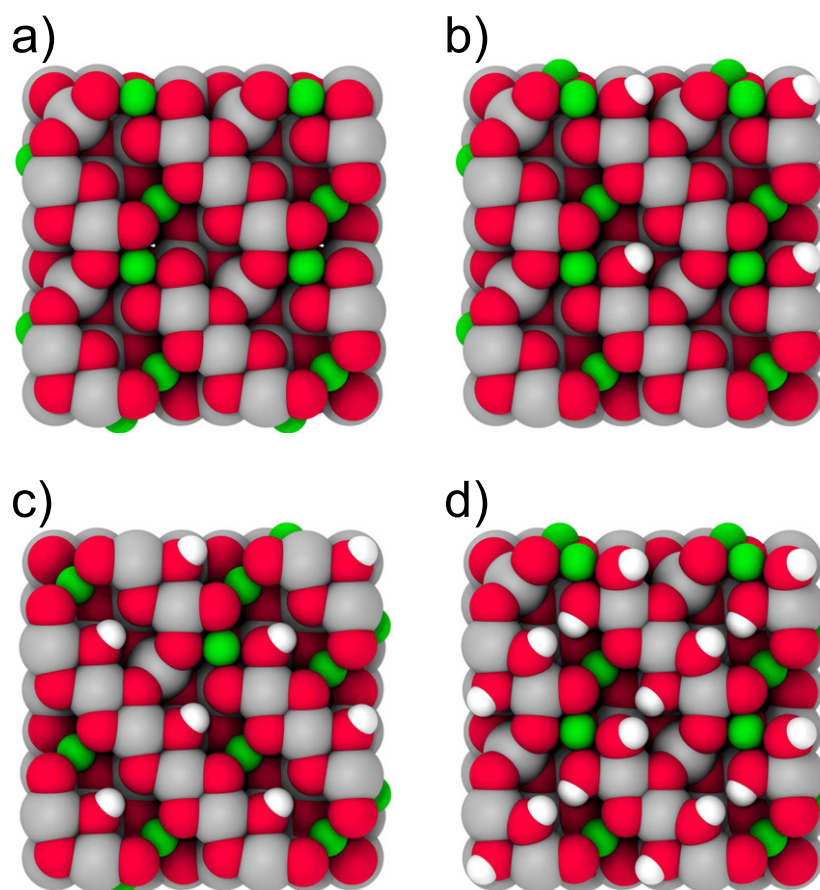


Figure 2. Possible configuration for $\text{MgAl}_2\text{O}_4(100)$ with inversion defects: (a) $\text{O}_4\text{-Al}_4\text{-O}_4$ termination with 50% inversions, (b) with 50% inversions and 1 H, (c) 12.5% inversions and 2 H, and (d) 50% inversions and 4 H per unit cell. The surfaces shown here represent the most stable configurations for the given amount of H adsorbed. Red atoms represents oxygen, grey is aluminum, green is magnesium and white represents hydrogen.

a non-equilibrium situation. The first concern is addressed by annealing the structures, enabling them to assume the most stable configuration. We cannot correct for the second concern, but we note that our conclusions are valid over several orders of magnitude of partial pressures and we believe them to be quite robust. Furthermore, we neglect the enthalpy and entropy contributions from the adsorbate vibrations. Calculating these would be time-consuming since they couple to the surface atoms and they remain a significant challenge for simulation methodology itself [35]. This approximation is expected to result in an underestimation of the stabilities of the surfaces with adsorbed hydrogen, i.e. these surfaces are probably slightly more stable than we calculate. In general, none of these issues affect our conclusions at all.

2.3. NC-AFM simulation

Non-contact AFM images were calculated using our home-built modular AFM simulator. The program integrates the discretized equation of motion of the cantilever taking into account the tip-sample interaction and the response of the model electronic set-up. The tip-sample interaction has to be calculated beforehand and fed to the program in a regular

data grid. A simple trilinear interpolation scheme is applied to extrapolate the values at the tip's position in every simulation step. We found that this simple interpolation method does not produce artificial features in the simulated images, provided that the grid is finer than the spatial resolution desired, and since the forces on the tip have to be evaluated at every simulation timestep, this method is also the fastest one. The cantilever is excited by its own signal (phase shifted by $\pi/2$) and an amplitude gain controller (AGC) adjusts the excitation intensity in order to keep the cantilever's amplitude at a constant setpoint. The cantilever's amplitude and frequency are measured by an amplitude demodulator and an analogue phase locked loop (PLL): implementation details can be found in section A. We simulated images in constant height mode, at different tip-sample separation, although here we show only the ones obtained at the distances that show best agreement with experiments. All our images are simulated at scanning speed $v = 10 \text{ nm s}^{-1}$.

2.4. Tip-sample interaction

Using DFT calculations, we calculated the interaction force between a model AFM tip and the sample. The originally silicon tip was contacted to the surface during scanning, and

is highly likely to have an apex covered with surface material. Since the tip remained stable during extensive imaging at small tip–surface distances, we can assume the apex has a high relative stability. Hence, it was modelled as an ideal $\text{Mg}_{32}\text{O}_{32}$ cube rotated around one corner: this allows us to select the atomic species at the apex, either Mg or O, providing a way to directly control the charge at the tip apex. The atoms in the 4 topmost layers of the cube are frozen, and all other atoms are allowed to relax—atomic displacements induced by the tip–surface interaction are key in high-resolution imaging [18]. For the sample surface, we use the same models adopted for the surface energy calculations described previously.

Force–distance curves are calculated by placing the tip above a specific point on the surface, where the initial height ($z = 0.5$ nm) is defined as between the relaxed position of the tip apex and the surface oxygen sublattice, and gradually approaching by 0.05 nm each step, while the electronic and atomic coordinates are relaxed, and the total force acting on the tip is recorded. Since this kind of calculation is quite expensive, we calculate force–distance curves only in relevant points of the surface unit cell, such as above the atoms and in the empty space between them. The number of force–distance curves required to have a reasonable estimate of the forcefield can be further reduced by taking into account the symmetry of the surface when possible. The computed forcefield is then interpolated and fed to the virtual AFM to produce the images. This step is not trivial due to the sparse arrangement of the calculated data points and the smoothness requirements of the interpolating function; a detailed explanation of the methodology is given in section B.

3. Results

3.1. Surface stability

Figure 3 shows a comparison of the surface energies for a variety of considered surface terminations calculated for the oxygen and hydrogen partial pressures used in the experiment as a function of the temperature. As presented in earlier work [19, 20], this analysis shows that the experimentally observed $\text{O}_4\text{-Al}_4\text{-O}_4$ termination becomes favoured over the magnesium termination (Mg_4) when the presence of oxygen is included in the analysis. Note that figure 3 also shows that oxygen vacancies (and Al vacancies) are energetically very unfavourable, and inversions are preferred at all temperatures considered. A top view ball model of the ideal $\text{O}_4\text{-Al}_4\text{-O}_4$ surface is illustrated in figure 1(a), which shows that this surface is composed of parallel rows of Al atoms (light grey, large) decorated by double rows of O atoms (red) and with Mg (green, small) atoms occupying half of the subsurface sites with a fourfold coordination to O. This surface further gains stability by forming so-called inversion defects created by the exchange of a surface Al with a subsurface Mg, as illustrated in figure 2(a), and the main remaining question is the role of hydrogen adsorbed on the surface.

The surface energy plot in figure 3 shows that adsorption of hydrogen on any of the surfaces clearly stabilizes it, allowing a further compensation method for the surface

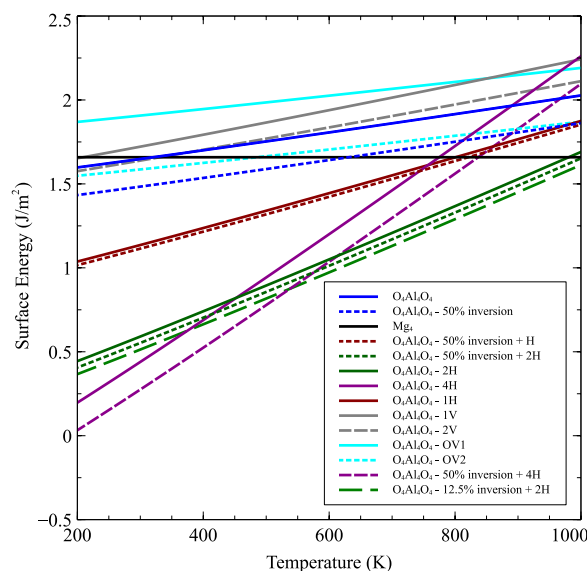


Figure 3. Calculated surface energies for a variety of surface terminations: $\text{O}_4\text{Al}_4\text{O}_4$ —oxygen-terminated surface (see figure 1(a)) also with 50% inversion defects (see figure 2(a)), and Mg_4 —Mg-terminated. 1V and 2V refer to single and double aluminum vacancies in the oxygen-terminated surface, while OV1 and OV2 refer similarly to oxygen vacancies (these are discussed in earlier work [20], and shown only for reference). 1H, 2H and 4H refer to the density of hydrogen on the surface, with 2H being equivalent to 25% coverage of the oxygen on the surface (see figure 1(c)). The partial pressures used for the calculations were 1×10^{-7} mbar for O_2 and 1×10^{-10} mbar for H_2 .

dipole [19, 20]. The calculations predict a H coverage of one ($\text{O}_4\text{-Al}_4\text{-O}_4\text{-1H}$ figure 1(b)) or two H atoms ($\text{O}_4\text{-Al}_4\text{-O}_4\text{-2H}$ figure 1(c)) per unit cell, to be favourable under the conditions of the experiment, with the higher density increasingly favoured at lower temperatures (figure 3) or higher H_2 pressures (not shown). We considered a large number of configurations of hydrogen adsorbed at these densities, and effectively the results are very similar; hydrogen always prefers to adsorb on the oxygen pair not bonded to subsurface Mg (see figure 1(d))—for 2H the difference is over 4 eV, reducing to just over 1 eV in 4H if half the H adsorbs near subsurface Mg.

The presence of the subsurface cation increases the coordination of the nearest oxygen, reducing the available bonding electrons and also repelling the similarly charged hydrogen. At 50% H density (4H), it is most favourable for hydrogen to bond to both atoms of this oxygen pair (figure 2(d)), forming a row of OH groups. The strong adsorption of H thus implies that the $\text{O}_4\text{-Al}_4\text{-O}_4$ termination with 25% H or more adsorbed on the oxygen atoms is predicted to be stable under the conditions of the experiment. At ambient or elevated pressure conditions relevant for the use of this material in e.g. catalysis a further stabilization of higher H coverages on the surface is predicted, but such conditions were not tested in the experiments [19].

3.2. Hydrogen diffusion

Earlier studies on other oxides demonstrate that hydrogen is often mobile at room temperature [36], especially when

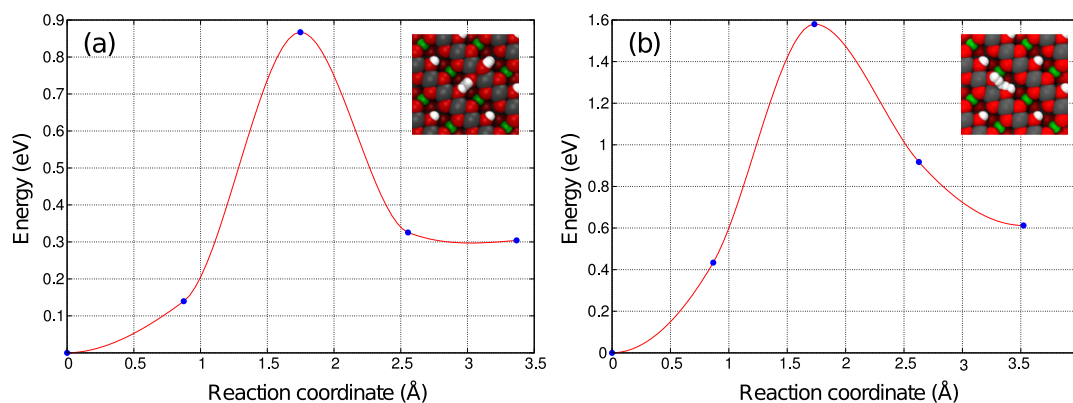


Figure 4. Calculated diffusion barriers for hydrogen moving on the $O_4Al_4O_4$ surface: (a) perpendicular to the aluminum rows, and (b) parallel to the aluminum rows.

influenced by the tip–surface interaction [37] or co-adsorbed with fast diffusing water species [38]. Figure 4 shows the diffusion barrier for hydrogen moving both perpendicular and parallel to the aluminum rows on the oxygen-terminated surface. Both barriers indicate that hydrogen should be rather immobile at room temperature. However, the barrier for diffusion across the Al row is of the order of 0.85 eV: the proximity of the tip is expected to lower this value, making diffusion thermally activated on the experimental timescale. The consequence of this would be that the contrast difference for the O pairs simulated for a 25% hydrogen coverage (2H) is smeared out in the direction perpendicular to the O rows and the image would therefore appear very similar to a 50% coverage (4H). The barrier for motion parallel to the O rows is almost double (1.6 eV), and is unlikely to be activated even by the presence of the tip.

3.3. NC-AFM simulations of surface OH groups

The theoretical analysis above thus shows that hydrogen present on the surface will be concentrated along the oxygen rows with a preference for the site without a neighbouring subsurface Mg. Experimental NC-AFM images of the plain $O_4Al_4O_4$ -terminated $MgAl_2O_4(100)$ surface are shown in figure 5. In general, two kinds of NC-AFM contrasts were observed on the non-defective parts of the surface and can be associated with the sign of the charge at the tip apex: scanning with a negatively terminated tip apex (figure 5(a)) yields a bright contrast for the (positive) surface Al lattice in the atom-resolved NC-AFM images, which appears as single atomic rows in the image whereas the O lattice are imaged with a dark contrast. In the complementary contrast mode recorded with the positive tip (figure 5(b)), the atomic resolution in the experimental NC-AFM image is located on the O atoms, and for close tip–surface distance the surface is imaged as bright O double rows whereas the darkest contrast is obtained on the Al rows. The surface point defects marked by dashed circles in both figures 5(a) and (b) are associated with the cation inversion sites illustrated in the calculations in figure 2(a). The additional presence of hydrogen on the surface implies that stationary OH groups situated on the

oxygen rows may modify the contrast in NC-AFM images, particularly for the positive tip where the NC-AFM contrast is located directly on the oxygen rows [19, 20]. From the experimental images, it is clear that any signature due to H is weaker than e.g. for the cation inversion defects. The detailed contrast modulation due to H in the NC-AFM images is, however, determined by a convolution of a geometrical effect due to the H protruding from O, relaxation of the H due to tip forces, and an electronic contribution from the nominally electropositive H.

First we check the influence of H on the ideal surface by simulating NC-AFM images on the $O_4-Al_4-O_4-2H$ termination (see figure 1(c)). Figure 3 shows that, in the absence of inversion defects, this surface is the most stable over most of the temperature range. At lower temperatures, $O_4-Al_4-O_4-4H$ becomes favourable, but several factors lead us to believe that 2H is equally, if not more, probable. Firstly, the difference in energies between the two structures is not large, and kinetic factors, such as steric effects (the energy gained by adsorption per H atom is 1 eV higher for 2H), may make the lower coverage more favourable. Secondly, the modulation seen in experimental images is fairly weak, and we would expect the presence of two H atoms in proximity to cause a larger change in contrast. Lastly, mobility of H at room temperature makes it difficult to distinguish between the two in AFM images in any case. Next, inversion defects are included and we consider the $O_4-Al_4-O_4$ surface with 50% inversions (figure 2(a)), as it is found to be the most stable H-free configuration. When H is also taken into account, we finally study the $O_4-Al_4-O_4-2H$ with 12.5% defects (figure 2(c)): this was chosen based on the arguments above and the fact that on the H-terminated surfaces lower inversion defect densities are predicted— $O_4-Al_4-O_4-2H$ with 12.5% is 0.8 eV lower in energy than $O_4-Al_4-O_4-2H$ with 50% (although we observe some preference for clustering of defects on the surface, but this is difficult to quantify within the limits of our simulation cell).

In the NC-AFM simulations, imaging the ideal $O_4-Al_4-O_4$ termination reveals the oxygen lattice when probed with the positive (Mg-terminated) tip (figure 6): the simulated images at close approach (figure 6(a)) reproduce the

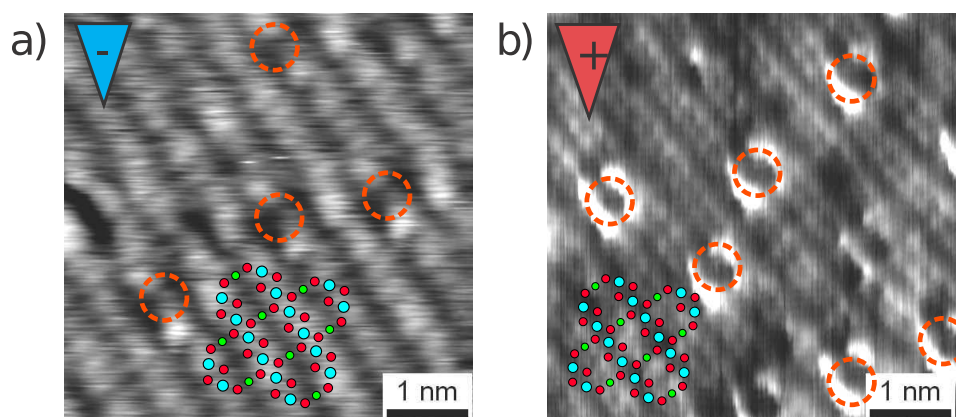


Figure 5. Atom-resolved constant height NC-AFM images of the $O_4Al_4O_4$ -terminated $MgAl_2O_4(100)$ surface measured with a negative (a) and positive (b) AFM tip apex (adapted from [19]; the red dashed circles mark the inversion defects). The superimposed ball models show the registry of the $O_4Al_4O_4$ surface in the respective images for the regions without apparent surface defects. Colour code: O (red), Al (large cyan), and (subsurface) Mg (green).

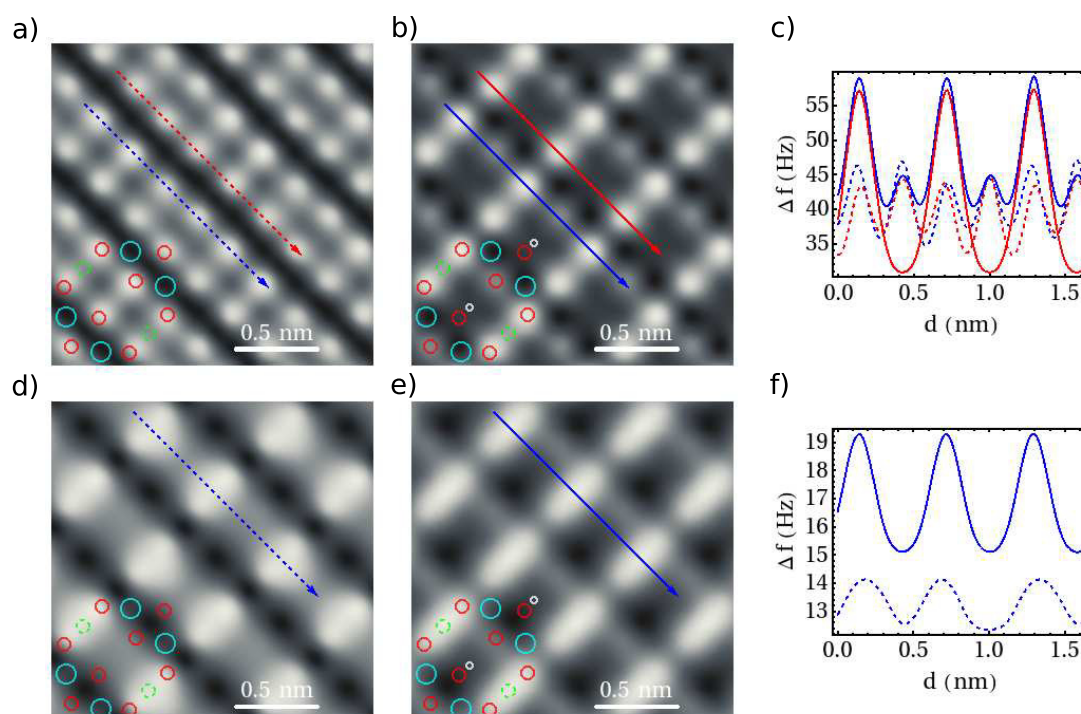


Figure 6. Images simulated with a positive tip on the ideal (a) and the hydroxylated (b) surfaces with the respective scanlines (c) obtained at a tip–sample distance of 2.6 Å. The images of the second row are calculated on the same surfaces at a tip–sample separation of 4 Å. The overlaid scheme shows O (red), Al (large cyan), H (small white) and Mg (green) atoms in their corresponding positions. Dashed circles represent atoms in the subsurface layer.

surface structure as two parallel stripes of protrusions, which is in excellent agreement with the experimental observation of defect-free areas on the surface as previously studied [19]. The O atoms appear similar, although the ones having a Mg atom in the sublattice are actually slightly brighter, as shown by the dashed scanlines in figure 6(c). The Al atoms can also be distinguished as forming dark rows in the image: the contrast there is significantly higher than in the empty regions between O rows. At larger tip–sample separation (figure 6(d)), the oxygen pattern is not atomically resolved: the contrast associated with the double oxygen rows is smeared out and it

appears as a single broadened row of protrusions with a faint double periodicity, reflecting the position of the subsurface Mg.

When the surface is hydroxylated (25% H coverage), the close approach image (figure 6(b)) reveals a modulation in the O pattern, where the contrast on the oxygen atom bound to H is significantly diminished due to a reduction of the effective charge seen by the tip; also the O opposite to it is less visible. On the other hand, oxygen atoms having Mg in the sublattice appear to interact more strongly with the tip, inducing a double periodicity along the oxygen rows. At larger

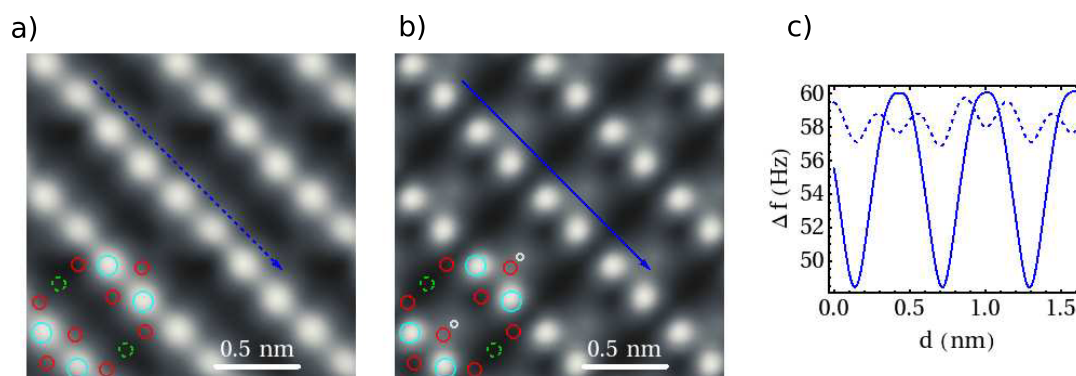


Figure 7. Images simulated with a negative tip on the ideal (a) and the hydroxylated (b) surfaces with the respective scanlines (c) obtained at a tip–sample distance of 2.6 Å. The overlaid scheme shows O (red), Al (large cyan), H (small white) and Mg (green) atoms in their corresponding positions. Dashed circles represent atoms in the subsurface layer.

distance (figure 6(e)), we observe a pattern similar to the ideal surface but the presence of H increases the overall contrast.

Simulating the O_4 – Al_4 – O_4 termination with the negatively terminated tip (figure 7(a)) shows the Al pattern on the surface, matching the experimental one, and from the scanline we see that each atom has a similar contrast. In the presence of H (figure 7(b)), the overall contrast is increased, and a feature appears at the H adsorption site, making the Al rows seem bridged. In both cases, O atoms cannot be directly resolved with the negatively terminated tip. In general, the effect of H is comparatively much weaker in this imaging mode, and therefore the strongest evidence for H is expected to be found when imaging with a positive tip. Our simulated images at larger tip–surface distance (not shown) showed only an overall decrease in contrast without significant changes in the pattern.

The NC-AFM contrast of the Mg surface site of a Mg–Al inversion defect is also influenced by H adsorbed on O. When antisite defects are included in the NC-AFM simulation of the ideal surface, half of the Mg atoms in the sublattice are switched with a neighbouring Al atom from the surface layers. A close approach simulation of this surface with a positive tip gives the image shown in figure 8(a): four defects are present in the simulated area. As in the ideal surface, oxygens sharing a sublattice Mg atom appear brighter than the others. At the antisite, where the sublattice has Al instead of Mg, a few O atoms interact less with the tip and appear darker than the others. The Al atoms appear as dark rows not atomically resolved, although the Mg defect site can be clearly spotted as a dark depression. When hydrogen adsorption on the O atoms neighbouring the antisite defect is taken into account, the most stable surface configuration has 12.5% inverted sites; therefore, only one defect is visible in our simulated images (figure 8(b)). The Mg defect along the Al row is still identified by a dark spot on the Al lattice (dark rows). However, compared to the ideal H-terminated surface, the contrast of O around the defects is changed: one of the O atoms around the defect appears in general much brighter whereas the contrast is lowered directly on the OH site. At larger distance, the presence of H is clearly visible as well. Without H, figure 8(d) shows the same features as the ideal

one, although the contrast on the O atoms directly above the defect is enhanced.

Simulations for the same surfaces with a negative tip give the images shown in figure 9. Without H, we see each Al atom with the same contrast, and the Mg antisite as a slightly weaker feature embedded in the Al row. Oxygen atoms cannot be individually seen and the area around the subsurface Al is slightly darker than the ideal surface case. Interestingly, when a H is added, the scanline in figure 9(c) indicates that there is still reduced contrast in one position along the Al row, and it does not correspond to the defect, but to one of the adjacent Al atoms; the inverted atom itself appears brighter than the rest of the Al row.

3.4. Experimental results

Figure 10(a) shows a positive tip NC-AFM image recorded at a relatively small (~ 2.5 Å estimated by comparison to simulations) tip–surface distance, where the double O row structure is still resolved. The circles superimposed on the image in the figure indicate the position of the Mg site in the Mg–Al inversion defects which are identified by the depression on the dark Al rows as seen in the simulations. Several of the defects are surrounded by a rim with very high intensity located on the six O atoms surrounding the defects, whereas for other defects the neighbouring O row structure appears much less unperturbed. This observation is in qualitative agreement with the expected contrast associated with the Mg–Al defects with and without H adsorbed, since the main effect of H is a relatively large contrast increase (up to 12 Hz in the experiment) on one of the surrounding O atoms next to the hydroxyl (figure 8(b)). The atomic resolution on the O atoms near the defect with a H adsorbed presents a contrast reduction, as predicted by the simulation, but less pronounced; it can be also noted how the apparent asymmetry associated with one of the O atoms neighbouring the hydroxyl being imaged as the brightest feature is clearly seen in the experiment. The experiment also shows that the increased intensity is located on both sides of most the Mg defects, whereas in the simulation it is confined only to the side with the H. This feature may be explained by a higher H coverage,

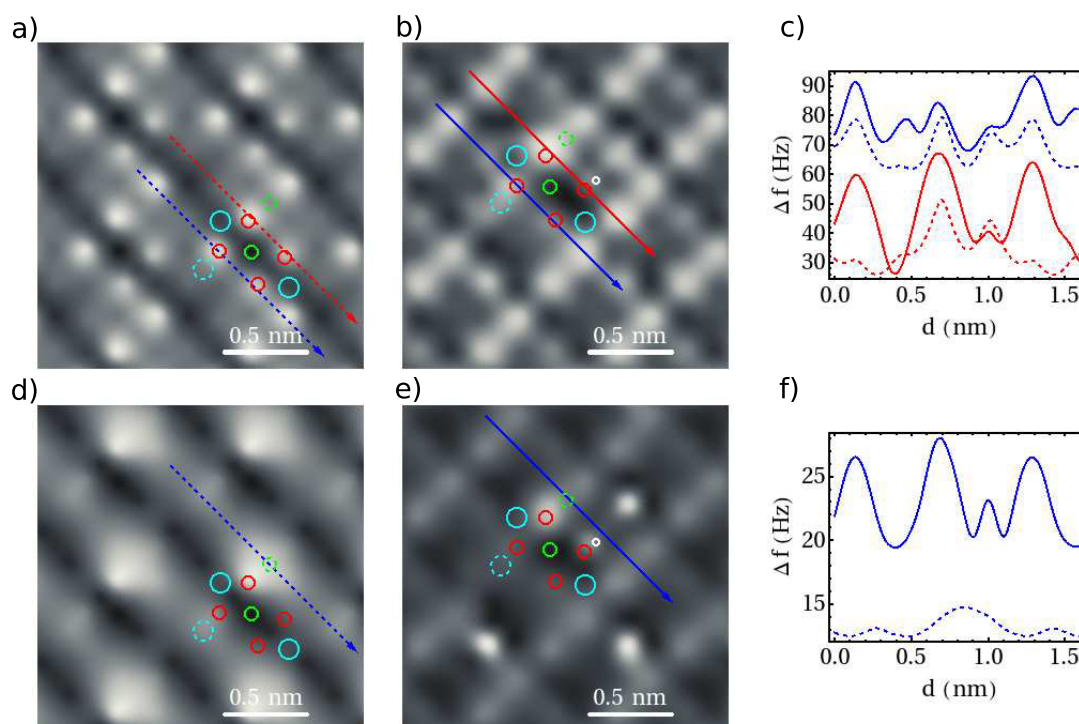


Figure 8. Simulated images on the MgAl_2O_4 surface in the presence of inversion defects obtained with a positive tip at a tip-sample distance of 2.6 Å ((a) and (b)) and 4 Å ((d) and (e)), and corresponding scanlines ((c) and (f)). The O–Al–O-terminated surface has 50% MG–Al inversions ((a) and (d)), while the H-terminated surface has 12.5% inversions. The overlaid scheme shows O (red), Al (large cyan), H (small white) and Mg (green) atoms in their corresponding positions. Dashed circles represent atoms in the subsurface layer.

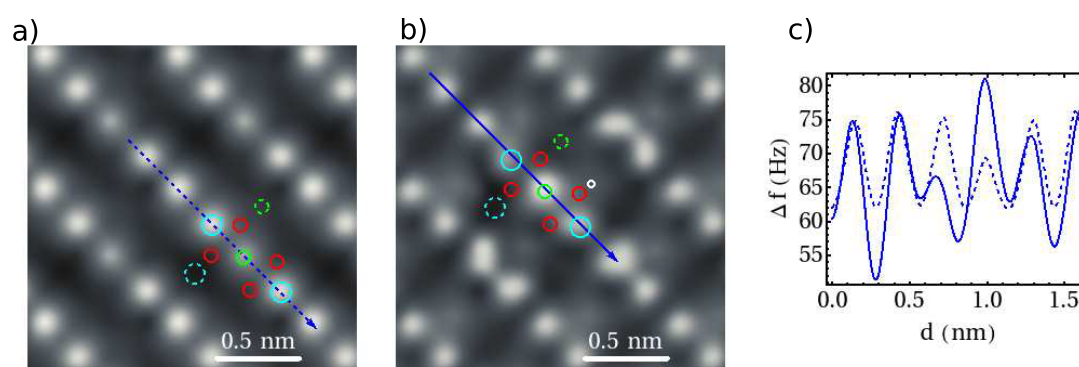


Figure 9. Images simulated with a negative tip on the ideal (a) and the hydroxylated (b) surfaces with the respective scanlines (c) obtained at a tip-sample distance of 2.6 Å. The overlaid scheme shows O (red), Al (large cyan), H (small white) and Mg (green) atoms in their corresponding positions. Dashed circles represent atoms in the subsurface layer.

i.e. clustering, at the defect site compared to the simulations, and it is in good agreement with the plot in figure 3 where the configurations with two or more H per defect site ($\text{O}_4\text{Al}_4\text{O}_4$ -50% inversion + 2H or 4H) are the most stable and the H atoms are located as OH groups on each side of the Mg. Additionally, we cannot exclude tip-induced mobility of the H across the Mg site on the Al row as the calculations suggested for the ideal surface in section 3.3.

As predicted by the surface energy calculations, evidence of H is found also in the defect-free regions of the surface. Here, the NC-AFM contrast associated with H appears less clear than on the defect site, but, as in the simulation, the linescan along the O rows (figure 10(c)) shows a downward modulation of the contrast on some sites of the O lattice, as

simulated in figure 6(b). Although the variations are small, we interpret such intensity variations as a plausible effect of H located as surface hydroxyls on the surface. As indicated in the linescan in figure 10(b), the reduction in the frequency shift is only 3 Hz on O sites, due to a slightly repulsive contribution to the total tip–surface force coming from the interaction between a positive tip and the positively charged H.

Similar effects are also observed for a large tip–surface separation in figure 11(a). At this imaging distance, the resolution of the double O rows is smeared out and they appear as broad single rows, and, in good agreement with the corresponding simulation in figure 6(d), the double periodicity along the bright O row becomes more pronounced. In

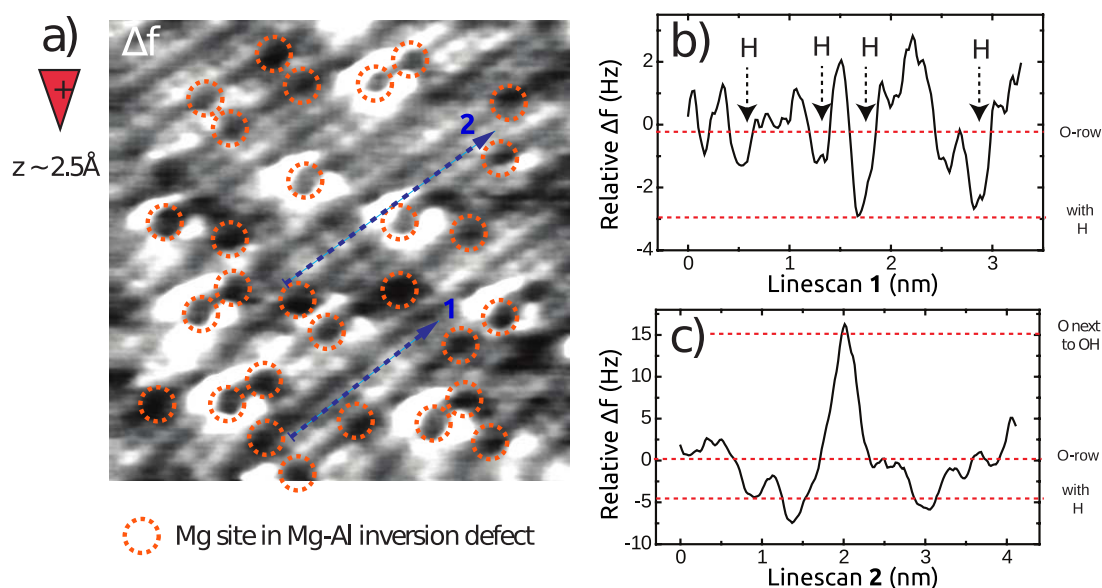


Figure 10. (a) A constant height NC-AFM image of the $O_4Al_4O_4$ -terminated surface recorded with a positively terminated tip apex at a short tip–surface distance (~ 2.5 Å). The size is 8×8 nm². $\Delta f_{\text{set}} = -138$ Hz, $V_{\text{gap}} = 3.0$ V, amplitude ~ 20 nm. Red circles indicate the position of the Mg atoms in the Mg–Al inversion defect. Linescans 1 and 2 shows the frequency variation relative to Δf_{set} along the line indicated in the image: (b) illustrates the contrast variation associated with H sites on the ideal surface, and (c) the contrast variation associated with H near a Mg defect site.

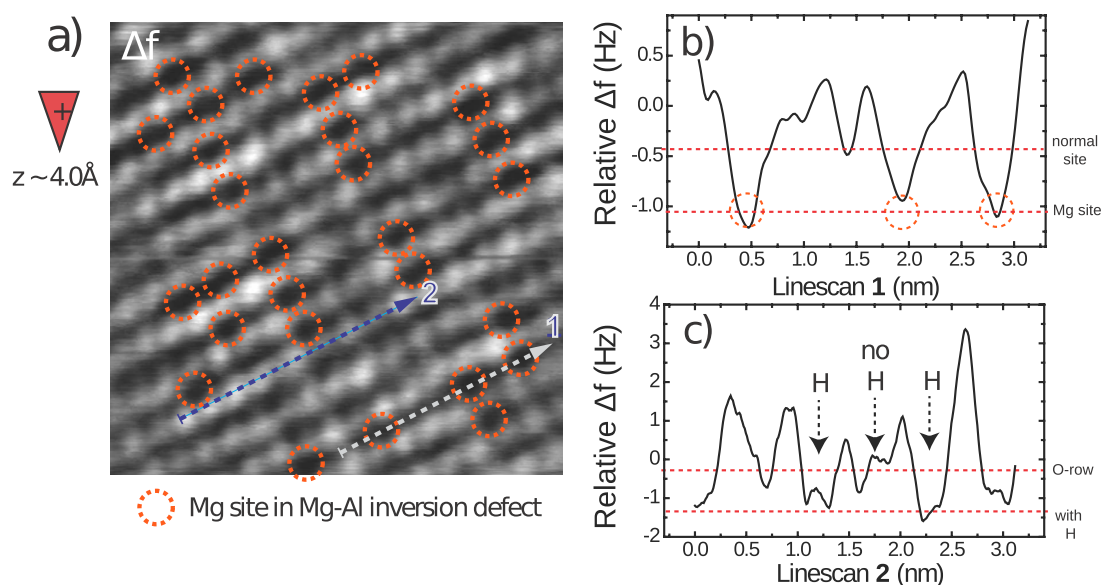


Figure 11. (a) A constant height NC-AFM image of the $O_4Al_4O_4$ -terminated surface recorded with a positively terminated tip apex at a ~ 4.0 Å tip–surface distance. Linescans 1 and 2 shows the frequency variation relative to Δf_{set} along the line indicated in the image: (b) illustrates a small ~ 0.5 Hz contrast variation on the dark Al lattice, which is tentatively associated with Mg sites of an inversion defect, and (c) the variation of the contrast associated with H.

addition, the experimental image in figure 11(a) shows that the Mg defect contour gets much weaker for large tip distances. The linescan in figure 11(b) shows a contrast variation on single sites of the order of 0.5–0.8 Hz along a line on the dark lattice. The presence of such dark sites on the Al lattice (shown by red circles in the images) is consistent with the simulation in figure 6(d) which shows that the overall darkest contrast should still be obtained on the Mg site of the inversion defect but with a much lower corrugation than for closer tip–surface distances.

The linescan in figure 11(c) shows the modulation of the contrast along the O rows. Furthermore, a lowered contrast on some sites is observed and it can be associated with H adsorption as calculated in figure 6(e). The simulation suggests that the double periodicity becomes strongly enhanced by the preferential adsorption of H on O sites with no neighbouring Mg in the subsurface layer, but this trend is not respected in the experiment where H seems to bind randomly with O sites regardless of their chemical environment. The discrepancy might be due to local variations in the H coverage (between 0 and 4 H per Al is possible in

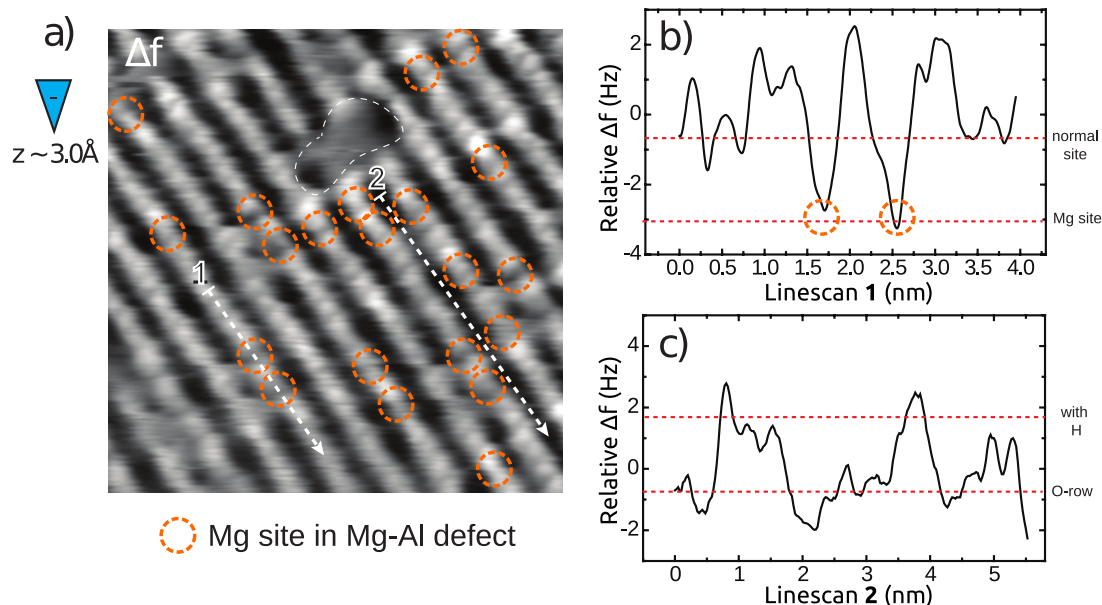


Figure 12. (a) A constant height NC-AFM image of the $O_4Al_4O_4$ -terminated surface recorded with a negatively terminated tip apex. The size is $9 \times 9 \text{ nm}^2$. $\Delta f_{\text{set}} = -35 \text{ Hz}$, $V_{\text{gap}} = 3.0 \text{ V}$, $A_{p-p} \sim 20 \text{ nm}$. Red circles indicate the position of the Mg atoms in the Mg–Al inversion defect. Linescan 1 shows the frequency variation relative to Δf_{set} along the line indicated in the image: (b) the contrast variation over two Mg defect sites, and (c) contrast variation on the dark O rows.: for.

figure 3) and the fact that the variation in the H adsorption energy is small ($\sim 0.41 \text{ eV}$) for each site compared to the total energy of adsorption of H (2.26 eV for Mg and 2.67 eV for non-Mg site gained per H) [19]. The signatures of H around the Mg site of the inversion defects becomes much weaker and the bright rim feature is not observed at this tip–surface distance, which is in agreement with the simulation.

Figure 12(a) shows an experimental NC-AFM image of the spinel surface recorded with a negative tip termination. Apart from a large unidentified defect in the upper half of the image, the Mg sites of the scattered inversion defects are identified by sites with a changed intensity on the clearly resolved Al lattice (indicated by red circles). The Mg defects are predicted in the simulation in figure 9 to appear as brighter protrusions at the defect site, or as a depression at the defect site followed by a brighter neighbouring Al, depending on whether the surface is clear or hydroxylated. Both types of contrast can be identified in the images, indicating whether H is present near the defect sites. An example of the latter type is shown in the linescan in figure 12(b), which shows a 2 Hz decrease followed by a general increase surrounding the defect site on the Mg sites. Furthermore, the bright Al rows are resolved and they appear to be bridged, as illustrated by the linescan in figure 12(c): this is in good agreement with the predicted increase in contrast after H adsorption both near defect sites and on the ideal surface.

4. Conclusions

The current paper has focused on the possible NC-AFM detection of surface OH groups that are predicted to be present on the $O_4Al_4O_4$ -terminated $MgAl_2O_4(100)$ surface. Experimental atom-resolved NC-AFM images show weak modulation on the contrast associated with either the Al lattice or O lattice of the surface, which indicated the presence

of H adsorbates. Simulated NC-AFM images on the ideal $MgAl_2O_4$ surface with H indeed give rise to features reflecting the preferential position of H on the O with no neighbouring Mg in the subsurface layer. Agreement between simulations and experiment is observed for isolated H atoms in both imaging modes, although the experimental features were always less visible than in the simulations. In addition, the simulations reflect a periodic arrangement of H, which could not be seen in the experiment. A possible explanation for the differences seen between experiment and simulations is that the assumption of a homogeneous coverage of hydrogen is incorrect due to kinetic factors involved in the hydroxylation process of the surface. Since the agreement in the appearance of inversion defects improves with the presence of hydrogen, it could be possible that hydrogen clusters around the inversion defects. Certainly the calculations predict that the surface with inversion defects gains $0.5\text{--}0.7 \text{ eV}$ by the adsorption of 1–3 hydrogens around the defect, but this results in a surface energy plot slightly less stable than the 1H configuration (see figure 3). A fully saturated surface with the ideal H coverage should be investigated in future NC-AFM experiments by dosing pre-dissociated H from a cracker source onto the surface. It is also likely that the presence of hydrogen is to some extent disguised by the inherent noise in the room temperature measurements, and future studies at low temperature, freezing in mobility and reducing the influence of co-adsorbed species should aid in fully resolving this question.

Acknowledgments

This work was supported in part by the Finnish Academy of Science and Letters. JVL and iNANO gratefully acknowledge support from Haldor Topsøe A/S and the European Research

Council (ERC Grant no. 239834, ‘Oxidesynergy’ (JVL)). FFC and ASF acknowledge support from the Academy of Finland via its Centre of Excellence programme and EU FP7 project MORDRED (grant no. 261868), as well as the computational resources offered by CSC, Finland.

Appendix A. Virtual AFM details

Our program allows us to build a virtual AFM starting from simple building blocks such as filters and controllers, making it possible to mimic the behaviour of the real experimental set-up. Here we explain how the different circuits of an AFM are modelled.

All low-pass filters in the virtual machine are modelled by the transfer function of an ideal Sallen–Key filter:

$$y(s) = G \frac{x(s)}{s^2 + \frac{\omega_c}{Q}s + \omega_c^2} \quad (\text{A.1})$$

where $x(s)$ and $y(s)$ are the input and output signal respectively, G is the gain, Q the quality factor, and ω_c the cutoff frequency. The filter is tuned to behave as a second order Butterworth filter by choosing $G = 1.5708$ and $Q = 0.7071$. The transfer function, expressed in the frequency-domain, is converted into the time-domain with a Laplace transform, and then discretized, so that at any simulation step the output of the filter can be calculated from the input and output values in the preceding two steps.

The amplitude demodulator (figure A.1) first takes the input signal and computes its absolute value, and then feeds the result to a low-pass filter with a cutoff frequency of 200 Hz. This method is valid only when the cantilever oscillates around $z = 0$, which we found to be the case in our simulations. The amplitude gain controller (AGC) is implemented as a proportional–integral controller that compares the measured amplitude to a setpoint value and gives an output $R(t)$ as follows:

$$R(t) = K_p(A_0 - A(t)) + K_i \int_0^t (A_0 - A(\tau)) d\tau \quad (\text{A.2})$$

where A_0 is the setpoint and K_p and K_i are the proportional and integral constant respectively. These constants are chosen to be stiff enough for the AGC to respond quickly to changes in amplitude, without inducing artificial oscillations in the output. The output signal $R(t)$ will be used as the amplitude for the excitation signal.

In our set-up, we decided to implement the self-excitation scheme, where the cantilever is driven by its own signal phase shifted by $\pi/2$. In practice we can normalize the cantilever’s velocity to an oscillation with unitary amplitude, and use it for excitation. If we assume the cantilever follows a harmonic trajectory, its velocity is also harmonic and it has always the correct phase shift, but its amplitude is proportional to the frequency. All we have to do is normalize the velocity signal and multiply it by $R(t)$ before using it as driving force. The cantilever’s frequency is tracked by an analogue PLL circuit, shown in figure A.2.

First, the cantilever’s signal and the reference oscillation coming from the voltage controlled oscillator (VCO) are

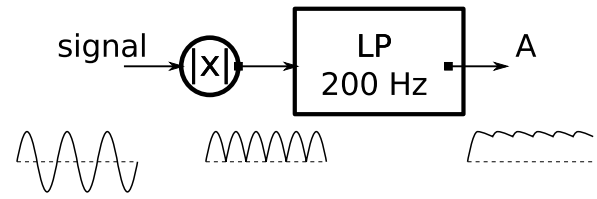


Figure A.1. Schematics of the amplitude demodulator. The wave forms illustrate the signal processing at each step.

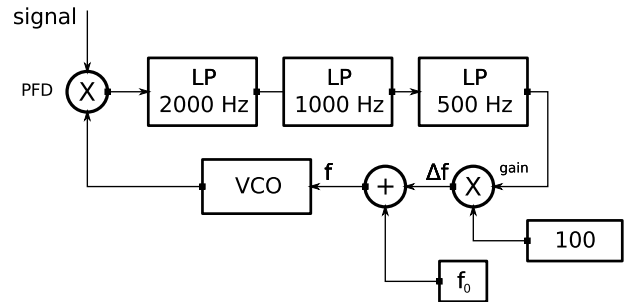


Figure A.2. Schematics of the analogue PLL circuit.

multiplied together by the phase-frequency detector (PFD). The resulting waveform is processed by a series of three low-pass filters with cutoff frequencies set to 2000 Hz, 1000 Hz and 500 Hz respectively, providing an estimate of the phase mismatch between the two oscillations. The mismatch is then amplified by a constant gain and used as the frequency shift to tune the frequency of the VCO itself. Note that this circuit is the main source of numerical error due to the discrete timestep. When the main and reference signals are multiplied in the PFD, the output wave contains a high frequency component at about $2f$, and even if the timestep is chosen to integrate correctly the cantilever’s trajectory, it might not be small enough to sample correctly higher frequencies. The error therefore propagates through the filters and induces an offset of a few Hz in the measured frequency shift. The error can be reduced by making the timestep smaller, thus increasing the computational time.

Appendix B. Forcefield interpolation

For this system, the forcefield computed with DFT is given as a collection of force–distance curves recorded in different key surface positions; therefore, the data points do not lie on a well structured grid along the x and y directions, but they are ordered along the z axis, since the force curves were all calculated at the same tip heights. Our goal is to represent the forcefield on a finer regular grid, so that the virtual AFM can use a fast trilinear interpolation algorithm to evaluate the tip–sample force at every timestep.

Since the data points are organized in z -layers, we call \vec{x}_i^k the position of the i th data point in the k th layer. We interpolate our sparse data along one xy plane with a smooth function giving the force in the k th layer as:

$$\vec{F}^k(\vec{x}^k) = \sum_i C_i^k d(\vec{x}^k, \vec{x}_i^k) \quad (\text{B.1})$$

where \vec{x}^k can be any point in the k th layer, $d(\vec{u}, \vec{v})$ is a kernel function, and C_i^k are numerical coefficients; the summation extends to all the data points in the layer. The kernel function is chosen as:

$$d(\vec{u}, \vec{v}) = \sqrt{\sum_c (u_c - v_c)^2 + h} \quad (\text{B.2})$$

where the sums runs over the spatial components of the vectors and $h = 0.5$ is a parameter used to obtain a smooth interpolation. The function $\vec{F}^k(\vec{x}^k)$ interpolates the data points only if:

$$\vec{F}^k(\vec{x}_j^k) = \sum_i C_i^k d(\vec{x}_j^k, \vec{x}_i^k) \quad (\text{B.3})$$

where $\vec{F}^k(\vec{x}_j)$ is the force calculated in \vec{x}_j . Solving this linear system gives the coefficients C_i^k in expression (B.1) to extrapolate the force in every layer. This interpolation scheme does not naturally feature periodic boundary conditions in the x and y directions, which are induced by considering a larger dataset, including the periodic replicas of the original one. The force between two interpolated layers is then given by linear interpolation between $\vec{F}^k(\vec{x})$ and $\vec{F}^{k+1}(\vec{x})$. Finally we evaluate the forcefield on a fine ($64 \times 64 \times 8$) regular grid above the surface and use it as input for the virtual AFM.

This approach could in principle be used to get a smooth interpolation of the whole forcefield, although our studies revealed this is not the optimal way to proceed. Points along the z direction are regularly spaced and few in number; also the characteristic shape of the force curves (rapidly changing repulsive and attractive parts followed by a flatter tail) often causes Runge's oscillation in the interpolation [39]. The linear interpolation along z does not present this issue, although the extracted force gradient is not continuous. We found this not to be a critical issue because the virtual AFM is operated at amplitudes much larger than the separation between points; thus, the cantilever feels an average of the force gradients in the interpolated region.

References

- [1] Hazen R M, Papineau D, Bleeker W, Downs R T, Ferry J M, McCoy T J, Sverjensky D A and Yang H 2008 *Am. Mineral.* **93** 1693–720
- [2] Fierro J L G (ed) 2006 *Metal Oxides—Chemistry and Applications* (Boca Raton, FL: Taylor and Francis)
- [3] Jackson S (ed) 2009 *Metal Oxide Catalysis* vol 2 (Weinheim: Wiley-VCH)
- [4] Rostrup-Nielsen J (ed) 1984 *Catalysis—Science and Technology* vol 5 (Berlin: Springer)
- [5] Papavasiliou J, Avgouropoulos G and Ioannides T 2007 *J. Catal.* **251** 7–20
- [6] Jacobs J, Maltha A, Reintjes J, Drimal J, Ponec V and Brongersma H 1994 *J. Catal.* **147** 294–300
- [7] Fang C M, Parker S C and de With G 2000 *J. Am. Ceram. Soc.* **83** 2082–4
- [8] Davies M J, Parker S C and Watson G W 1994 *J. Mater. Chem.* **4** 813–6
- [9] Bragg W G 1915 *Phil. Mag.* **30** 305
- [10] Sickafus K E, Wills J M and Grimes N W 1999 *J. Am. Ceram. Soc.* **82** 3279–92
- [11] Fang C M, de With G and Parker S C 2001 *J. Am. Ceram. Soc.* **84** 1553–8
- [12] Fang C M, Parker S C and de With G 2001 *Key Eng. Mater.* **206–213** 543–6
- [13] Laag N J V D, Fang C M, With G D, Wijs G A D and Brongersma H H 2005 *J. Am. Ceram. Soc.* **88** 1544–8
- [14] Laag N J V D, Dijk A J M V, Lousberg N, With G D and Dortmans L J M G 2005 *J. Am. Ceram. Soc.* **88** 660–5
- [15] Yanina S V and Carter C B 2002 *Surf. Sci.* **513** L402–12
- [16] Giessibl F 2003 *Rev. Mod. Phys.* **75** 949
- [17] Barth C, Foster A S, Henry C R and Shluger A L 2011 *Adv. Mater.* **23** 477–501
- [18] Hofer W, Foster A and Shluger A 2003 *Rev. Mod. Phys.* **75** 1287–331
- [19] Rasmussen M K *et al* 2011 *Phys. Rev. Lett.* **107** 036102
- [20] Rasmussen M, Foster A, Canova F, Hinnemann B, Helveg S, Meinander K, Besenbacher F and Lauritsen J 2011 *Phys. Rev. B* **84** 235419
- [21] Morterra C, Ghiotti G, Boccuzzi F and Coluccia S 1978 *J. Catal.* **51** 299–313
- [22] Rossi P F, Busca G, Lorenzelli V, Waqif M, Saur O and Lavalley J C 1991 *Langmuir* **7** 2677–81
- [23] Lauritsen J V and Reichling M 2010 *J. Phys.: Condens. Matter* **22** 263001
- [24] Kerber S J, Bruckner J J, Wozniak K, Seal S, Hardcastle S and Barr T L 1996 *J. Vac. Sci. Technol. A* **14** 1314–20
- [25] Lauritsen J V *et al* 2011 *ACS Nano* **5** 5987–94
- [26] Yamamoto S, Bluhm H, Andersson K, Ketteler G, Ogasawara H, Salmeron M and Nilsson A 2008 *J. Phys.: Condens. Matter* **20** 184025
- [27] Kresse G and Furthmüller J 1996 *Comput. Mater. Sci.* **6** 15
- [28] Kresse G and Furthmüller J 1996 *Phys. Rev. B* **54** 11169
- [29] Blöchl P E 1994 *Phys. Rev. B* **50** 17953
- [30] Kresse G and Joubert D 1999 *Phys. Rev. B* **59** 1758
- [31] Henkelman G, Uberuaga B P and Jónsson H 2000 *J. Chem. Phys.* **113** 9901
- [32] Wang X G, Chaka A and Scheffler M 2000 *Phys. Rev. Lett.* **84** 3650–3
- [33] Reuter K and Scheffler M 2003 *Phys. Rev. Lett.* **90** 046103
- [34] Chase M W 1998 *J. Phys. Chem. Ref. Data* **9** 1–1961
- [35] Kurtén T and Vehkamäki H 2008 *Adv. Quantum Chem.* **55** 407
- [36] Martin D and Duprez D 1997 *J. Phys. Chem. B* **101** 4428–36
- [37] Enevoldsen G, Pinto H, Foster A, Jensen M, Hofer W, Hammer B, Lauritsen J and Besenbacher F 2009 *Phys. Rev. Lett.* **102** 136103
- [38] Wendt S, Matthiesen J, Schaub R and Vestergaard E 2006 *Phys. Rev. Lett.* **96** 066107
- [39] Runge C 1901 *Z. Math. Phys.* **46** 224